ACS Energy LETTERS

http://pubs.acs.org/journal/aelccp

Crowding Agent Stabilizes Aqueous Electrolyte for Reversible Iron Metal Anode

Louisa C. Greenburg, John Holoubek, Yi Cui, Pu Zhang, Huayue Ai, Elizabeth Zhang, Chenwei Liu, Guangxia Feng, and Yi Cui*

Cite This: *ACS Energy Lett.* 2025, 10, 1022−1029 Read Online

ABSTRACT: Aqueous batteries with Fe metal anodes are a promising technology for safe, low-cost stationary storage. Fe can deliver high gravimetric and volumetric capacities, but its commercial viability is hindered by competing side reactions and low Coulombic efficiency. This work explores the feasibility of employing polyethylene glycol (PEG) as a crowding agent in Fe electrolyte to suppress the competing hydrogen evolution reaction (HER) and improve Fe plating/stripping efficiency. We demonstrate that in a 1 molal Fe electrolyte, employing 60% PEG/40% H_2O as the solvent yields higher Coulombic efficiency in Fe||Cu half cells and enables over two times the cycle life in Fe||Fe symmetric cells compared to the control composed of 100% H_2O solvent. Further, we find that the 60% PEG electrolyte decreases H_2 generation by almost 10 times during cycling. This electrolyte engineering approach also yields more crystalline Fe nuclei and denser growth during plating, leading to highly compact and reversible Fe anodes. Our results encourage further development of molecular crowding electrolytes for high efficiency Fe metal anodes.

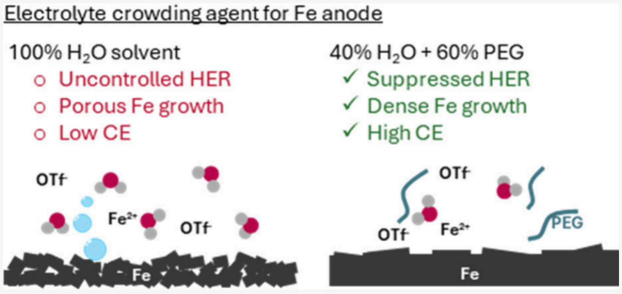

Lithium-ion batteries (LIBs) are a leading energy storage technology, with applications in mobile devices, electric vehicles, and stationary storage. However, the limited availability of lithium and its increasing cost present major concerns for the proliferation of battery storage. In addition, the flammable organic electrolytes pose safety issues, which also contribute to a consumer aversion of battery products.

Aqueous batteries based on more abundant charge carriers present an alternative to traditional organic-based LIBs, especially for stationary storage applications. These systems utilize nonflammable water as the electrolyte solvent and can utilize cheaper, more abundant metals such as zinc, iron, or aluminum instead of lithium. While Zn has been a leading subject of aqueous battery anode research, Fe is more naturally abundant (~50000 ppm in Earth's crust compared to ~80 ppm of Zn)[1] and even lower cost.[2−4] After ore reduction, Fe is over 7x cheaper than refined Zn.[5,6] Fe also has a higher theoretical capacity of 960 mAh g^{-1}, or, volumetrically, 7557 mAh cm^{-3}.[2,7]

However, several issues impede the progress of the Fe anode. In acidic electrolyte, the Fe metal anode operates by a plating/stripping mechanism: $Fe^{2+} + 2e^- \leftrightarrow Fe^0$ (−0.44 V vs standard hydrogen electrode (SHE)).[2] Low efficiencies arise from competition between the Fe^{2+}/Fe redox reaction and the hydrogen evolution reaction (HER): $2H^+ + 2e^- \rightarrow H_2$.[8] Further, unlike the better-explored Zn metal anode, which is anticatalytic toward hydrogen evolution, Fe has catalytic properties that accelerate HER.[9] As a result, once Fe starts plating, the HER can happen more rapidly. This issue is made worse by the characteristically high overpotential required to plate Fe, thus providing even more driving force for HER.[1,10,11] In addition to low efficiency, undesirable high surface area Fe morphology is often observed which provides even more sites for hydrogen evolution.[3] Recent work has demonstrated the mitigation of these issues via electrolyte engineering, such as adding high concentrations of metal chloride salts into the electrolyte[12,13] or ZnI_2 additives that enable doping of Zn into the Fe lattice.[14] However, other strategies to improve Fe plating and stripping in acidic aqueous batteries remain relatively unexplored.

A promising approach to suppress HER is to disrupt the hydrogen-bonding network of the water solvent.[15] If the intermolecular H-bonds of water molecules can be weakened, then the covalent O−H bond within a water molecule can be strengthened, which increases the HER overpotential. This

Received: November 25, 2024
Revised: January 27, 2025
Accepted: January 30, 2025
Published: February 3, 2025

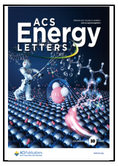

https://doi.org/10.1021/acsenergylett.4c03268

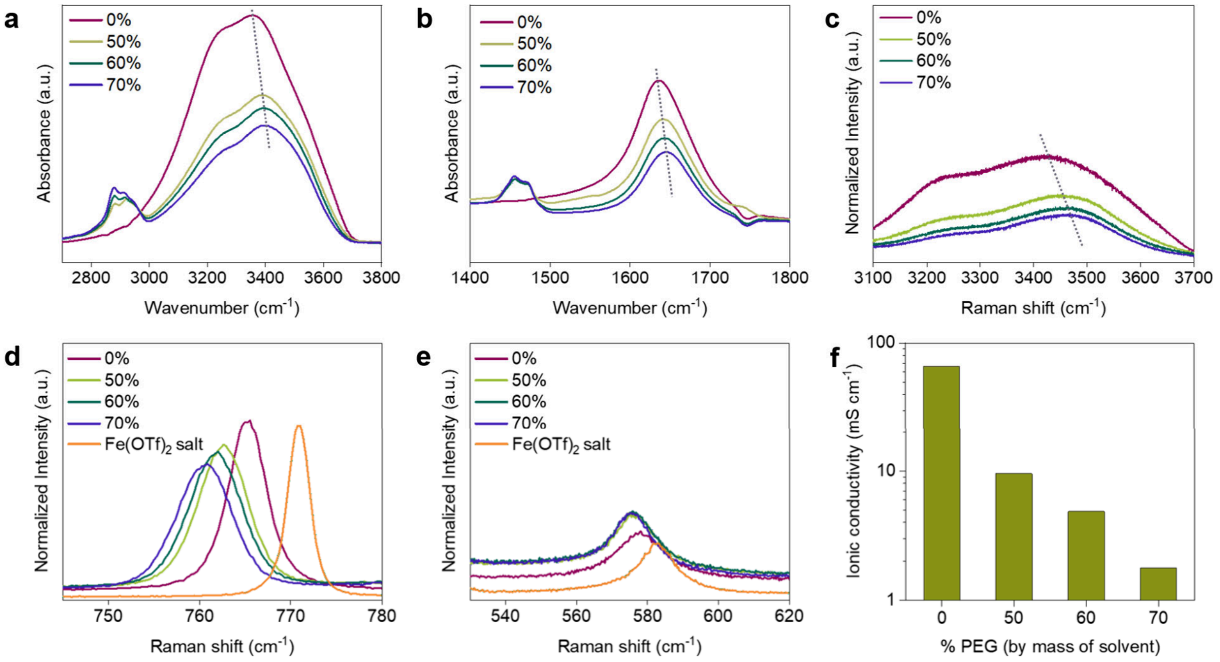

Figure 1. Properties of aqueous Fe electrolytes. For 1 m Fe(OTf)$_2$ with varying PEG composition (0%, 50%, 60%, and 70% PEG by mass of solvent, remainder is water): a) FT-IR absorption peak of O−H stretching of water; b) FT-IR absorption peak of O−H bending of water; c) Raman spectra of O−H stretching in water; d) Raman spectra of $\delta_s(CF_3)$ band from OTf$^-$ anion; e) Raman spectra of $\delta_{as}(CF_3)$ band from OTf$^-$ anion; f) ionic conductivity of the four electrolyte systems.

effect was demonstrated in aqueous lithium batteries using low molecular weight polyethylene glycol (PEG) as a cosolvent to disrupt water's intermolecular bonding and increase its electrochemical stability window.[15] Since then, this strategy, termed "molecular crowding" has been successfully employed for Zn metal using a variety of crowding agents.[16−23] In this work, we explore the usefulness of this approach for Fe metal anodes and study its effect on Fe nucleation and growth. We use the inexpensive PEG-400 as a cosolvent to water in slightly acidic electrolyte with iron(II) trifluoromethanesulfonate (Fe(OTf)$_2$) salt. The electrolyte is characterized to understand the effect of PEG on the bonding environment within the Fe-based electrolytes, and we evaluate the performance of a series of PEG-400 electrolytes in half- and symmetric cells. We measure the hydrogen generated after 10 cycles and find that PEG-400 suppresses the HER, leading to increased plating/stripping efficiency for the Fe metal anode and more compact Fe nucleation and growth.

To understand the effect of PEG (molecular weight ∼400 g/mol) as an electrolyte component for aqueous Fe electrolytes, we mixed four solutions of deionized water and PEG-400 with the following amounts of PEG by mass: 0%, 50%, 60%, and 70%. These ratios were selected to explore a balance between high cation mobility in water and potential benefits imparted by PEG. To each solution was added Fe(OTf)$_2$ to make a concentration of 1 molality each. This salt is chosen for its considerable solubility in PEG/H_2O and possibility to contribute to an OTf$^-$ derived solid electrolyte interphase.[24] Using Fourier transform infrared (FT-IR) spectroscopy, we first observed how bond strengths change with the addition of PEG. Figure 1a depicts the absorption peak of the O−H stretching in water. As the PEG content increases from 0 to 70%, we observe a blueshift in the absorption peak (from ∼3358 cm^{-1} to ∼3400 cm^{-1} with 0 to 70% PEG respectively), suggesting that the covalent O−H (H_2O) bond is strengthened with the increase in PEG content.[15] The same effect is observed in Figure 1b, in which water's O−H bending peak without PEG is at ∼1635 cm^{-1} and shifts to 1646 cm^{-1} with 70% PEG. As expected, increasing PEG content gives higher peak intensity at 2879 cm^{-1}, which corresponds to the C−H stretching of PEG and at 1456 cm^{-1}, which corresponds to the C−H bending,[15] whereas the 0% PEG electrolyte does not have peaks at these wavenumbers.

Raman spectroscopy also supports the FT-IR result: within the O−H (H_2O) stretching band between 3100 and 3700 cm^{-1}, there is a gradual blueshift as PEG content increases, associated with the disruption of the intermolecular H-bond network and strengthening of O−H bonding within individual water molecules (Figure 1c).[21] The region at ∼2700 to 3000 cm^{-1} corresponds to the symmetric C−H stretching vibration of PEG which increases in intensity as PEG content increases. Interestingly, when compared to neat PEG-400 without any salt or water added (Supplementary Figure 1), the PEG electrolytes exhibit a significant increase in the relative intensity of the peak at ∼2922 cm^{-1} vs the peak at ∼2886 cm^{-1}.This has been previously observed in PEG/water solutions and may be attributed to hydrogen bonding solvent interactions affecting a CH_2 stretching mode or a Fermi resonance.[25]

We can also use Raman spectroscopy to explore the effect of the solvents on the Fe salt. We observe the symmetric angle deformation of CF_3 ($\delta_s(CF_3)$) in the OTf$^-$ anion at ∼762 cm^{-1} (Figure 1d).[26] This region gives us information about anion coordination. The solid Fe(OTf)$_2$ salt yields the highest wavenumber $\delta_s(CF_3)$ band, which exhibits a red shift when dissolved in water. As PEG is added, the $\delta_s(CF_3)$ band shifts to even lower wavenumbers. This red shift suggests an increase in OTf$^-$/PEG interactions as OTf$^-$/H_2O interactions are reduced.[27,28] We observe the same effect in the Raman spectra

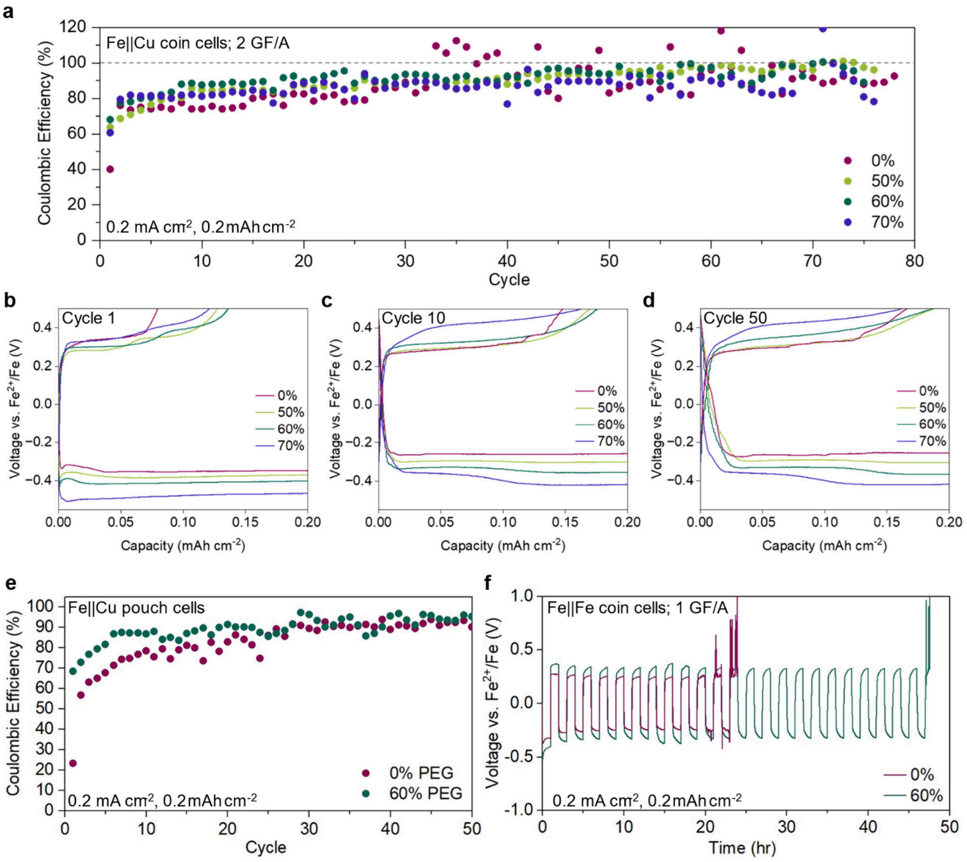

Figure 2. Electrochemical performance of Fe metal anode with varying PEG content in the electrolyte. a) Coulombic efficiency of Fe||Cu coin cells with 0%, 50%, 60%, and 70% PEG by mass of electrolyte solvent. A dashed line is drawn at 100% CE for clarity. Corresponding voltage profiles of the Fe||Cu coin cells for the b) first, c) tenth, and d) fiftieth cycle. e) Coulombic efficiency of Fe||Cu pouch cells with 0% and 60% PEG. f) Voltage vs time profile of Fe||Fe coin cells with 0% and 60% PEG electrolyte and one glass fiber (GF/A) separator per cell to accelerate failure.

of the $-CF_3$ asymmetric deformation mode ($\delta_{as}(CF_3)$) (Figure 1e).

These FT-IR and Raman results are promising for achieving HER suppression. The strengthening of the O−H bonds in water should require a higher driving force for the HER, thus making Fe plating relatively more favorable. A drawback to this approach, however, is that PEG-400 is a viscous liquid, and increasing PEG content decreases the ionic conductivity of the electrolyte (Figure 1f). With 0% PEG, the ionic conductivity of the 1 mol of $Fe(OTf)_2$ electrolyte is 65 mS cm^{-1}. From 50 to 60 to 70% PEG, this value drops to 10, 5, and 2 mS cm^{-1} respectively. The ionic conductivity is negatively correlated to the viscosity, which increases with PEG content (Supplementary Figure 2). Thus, there is a trade-off between O−H bond strength and ionic conductivity for this electrolyte system.

Despite the reduced conductivity, the evidence of water's intramolecular O−H bond strengthening is encouraging for the Fe metal anode performance. First, we used the 60% PEG system to confirm that PEG does not alter the acidic electrolyte's Fe plating/stripping mechanism. We assembled three Fe||Cu half-cells and used X-ray diffraction (XRD) to measure the Cu electrodes from each cell. In the first cell, we plated 0.4 mAh Fe cm^{-2} onto the Cu substrate. In the second cell, we plated the same capacity and stripped to 0.5 V, and in the third cell, we plated, stripped, and then plated 0.4 mAh cm^{-2} again (Supplementary Figure 3). We can clearly observe the emergence of Fe metal peaks on the Cu foil after each plating and their near disappearance after stripping, confirming that the plating/stripping reaction is occurring in the PEG electrolyte. With XRD, we also confirm Fe metal plating in the 0% PEG electrolyte (Supplementary Figure 4).

To understand how these electrolytes affect the efficiency of the Fe^{2+}/Fe redox reaction, we assembled Fe||Cu half-cells with each of the four electrolyte solutions. As depicted in Figure 2a, the 0% PEG electrolyte yields the lowest first cycle Coulombic efficiency (CE) of 40%, while the 60% PEG system exhibits the highest first cycle CE of 68%. The 70% PEG electrolyte reaches a 60.1% initial CE, which is just below that of the 50% PEG system, which delivers 64.5% initial CE. Notably, the 0% PEG electrolyte has the lowest plating overpotential on the first cycle (Figure 2b) likely due to its highest ionic conductivity, whereas increasing PEG content increases the overpotential as ionic conductivity is decreased. Interestingly, the 0% PEG has a first cycle stripping potential similar to that of the 70% PEG electrolyte.

After the first cycle, the plating overpotentials decrease in all systems, and the CEs rise. Additional plateaus appear in the stripping profile of 0% PEG as shown in Figure 2c for cycle 10. These plateaus may be from contact issues, soft shorting, or side reactions, as supported by its unphysical >100% CE[29] first observed at cycle 33 and the unstable voltage profiles, also shown for cycle 50 (Figure 2d). Meanwhile, the PEG-based electrolytes exhibit more stable voltage profiles and CE values.

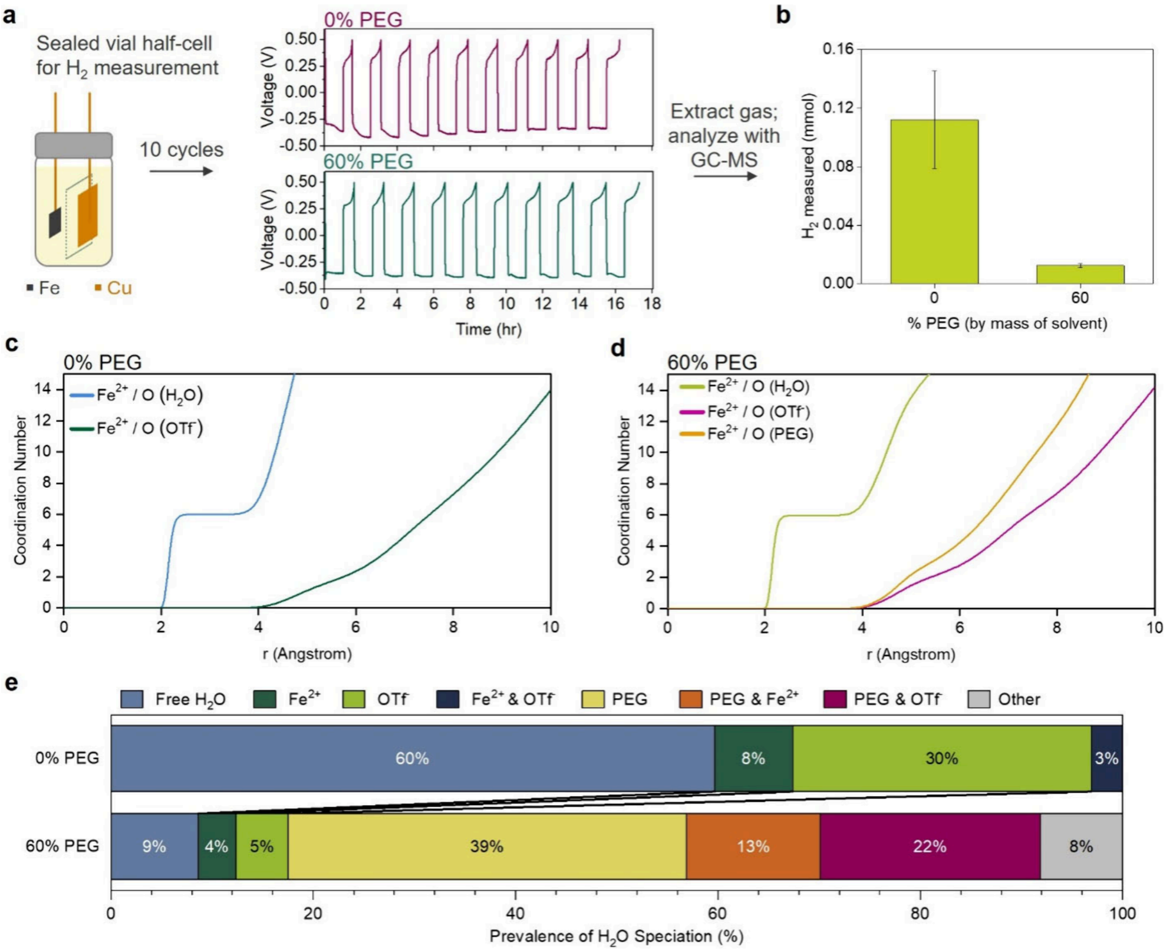

Figure 3. H_2 evolution and species solvation in 0% and 60% PEG electrolyte. a) Fe|Cu half-cells made in GC vials and sealed to keep all gases in, followed by 10 cycles of Fe plating and stripping, before gas analysis via GC-MS. b) H_2 (mmol) measured by GC-MS from vial cells after cycling in the 0% and 60% PEG electrolytes. Coordination number distribution functions calculated from MD simulations for c) 1 m $Fe(OTf)_2$ in 0% PEG/100% H_2O and d) 1 m $Fe(OTf)_2$ in 60% PEG/40% H_2O. e) Prevalence of H_2O solvation for the 0% and 60% electrolytes; the percentages indicate the percent of H_2O in system that solvates the electrolyte component indicated in the legend.

The 60% PEG is the first to reach >90% CE at cycle 18, at which point the 70%, 50%, and 0% electrolytes have a CE of 82.7%, 82.1%, and 76% CE respectively. Overall, 60% PEG gives the highest average CE with stable voltage profiles, implying that its solvent ratio best optimizes the trade-off between efficiency and overpotential increases. Because the 60% PEG electrolyte appears to be the most promising, we focus on comparing this system to the control 0% PEG electrolyte for the remainder of the study.

The Fe|Cu coin cells utilize stainless steel metal casings, which may provide more active sites for the HER. To better understand the effect of the electrolyte on Fe plating without metal casings, we assembled pouch cells with the 60% PEG and the control 0% PEG electrolytes. As shown in Figure 2e and Supplementary Figure 5, we find that the 60% PEG performs similarly in the pouch half cell compared to the coin cell. The first cycle CE in the pouch is 68.45% compared to 68% in the coin cell. The control pouch falls to 23.3% first cycle CE compared with 40% in the coin cell. The overall trend of higher CE in the 60% PEG system is maintained, suggesting that the Fe anode (rather than the stainless steel alone) serves as active sites for the HER that contributes to lower CE in the 0% PEG system.

Next, we assembled Fe|Fe symmetric coin cells. Instead of using 2 GF/A glass fiber separators as done to this point, we used just 1 separator to accelerate the failure of the cells. We find that at 0.2 mA cm^{-2} and 0.2 mAh cm^{-2}, the 0% PEG cell begins to soft-short after only 20 h and can no longer run after 24 h (Figure 2f). The 60% cell lasts over twice as long, running smoothly for 48 h. When two separators are used, the 60% PEG electrolyte runs without shorting for at least 900 h (Supplementary Figure 6). We note that in the PEG system, an additional plateau develops at −0.2 V with cycling (Supplementary Figure 7). Two plateaus have been previously observed during metal plating in water/PEG systems,[30] and future work should focus on understanding the aging of the Fe anode in such systems.

While CE values and the corresponding voltage profiles give us an initial understanding of Fe anode efficiency, we can directly measure the hydrogen generation that occurs during Fe plating and stripping by using gas chromatography (GC). We fabricated Fe|Cu half cells in sealed GC vials, which we cycled for 10 plating and stripping cycles with the same current parameters as used previously (0.2 mA cm^{-2}, 0.2 mAh cm^{-2}) (Figure 3a). After cycling, we extracted the gas and analyzed it by using GC-mass spectrometry (Figure 3b). On average, the 0% PEG system generated 0.112 mmol of H_2 gas during the

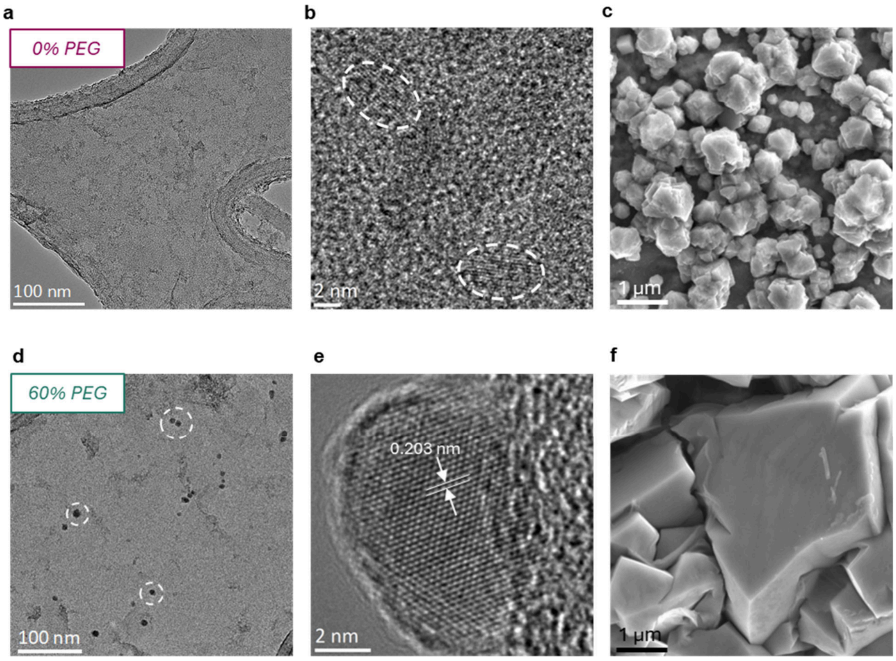

Figure 4. Nucleation and growth of Fe. In the 0% PEG system: a) high resolution TEM of 5 μAh cm^{-2} Fe plated at 0.2 mA cm^{-2}. b) Higher magnification TEM revealing highly disordered crystalline regions. c) SEM of high surface area Fe after plating 3 mAh cm^{-2} at 0.2 mA cm^{-2}. In the 60% PEG system: d) high resolution TEM of 5 μAh cm^{-2} Fe plated at 0.2 mA cm^{-2}. e) higher magnification TEM revealing highly crystalline α-Fe nuclei. f) SEM of compact Fe after plating 3 mAh cm^{-2} at 0.2 mA cm^{-2} in the 60% PEG system.

ten cycles, whereas the 60% PEG system averaged 0.0124 mmol, representing a nearly 10x reduction in hydrogen evolution when 60% PEG is introduced. Thus, we confirm that PEG suppresses the HER, thereby minimizing the side reactions and allowing higher efficiency Fe plating. This result is consistent with the FT-IR and Raman data, which suggested that the PEG electrolytes would have higher HER overpotential due to the increased O−H bond strength of water (imparted by the PEG).

With evidence that PEG suppresses HER during Fe plating/stripping, we next turn to molecular dynamic (MD) simulations to further investigate how PEG affects Fe^{2+} solvation and the electrolytes' intermolecular interactions. Snapshots of the MD simulation in 0% and 60% PEG are presented in Supplementary Figures 8a and 8b. We obtained the radial distribution functions (Supplementary Figures 8c and 8d) and coordination number distribution functions (Figure 3c and Figure 3d) from these MD simulations. In both electrolytes, Fe^{2+} is solvated by six H_2O molecules on average. Significant differences in the cation−anion pairing are not observed between the 0% and 60% PEG cases. The primary difference in Fe^{2+} solvation is that the 60% PEG electrolyte introduces some PEG into the second solvation shell, yet any effect on proton acidity in first shell H_2O remains unclear. Rather, the water molecules that solvate Fe^{2+} are themselves less solvated by other water molecules in the 60% PEG compared to in the 0% PEG electrolyte, which highlights the effectiveness of PEG in disrupting H_2O−H_2O H-bonding. In Li batteries, it is typically desired to have more anions in the Li$^+$ solvation shell to create a more robust, inorganic solid electrolyte interphase (SEI),[31−34] but the existence of an SEI on Fe anodes is not well understood. Plus, more hydrated cations might exhibit higher mobility compared to cations solvated by bulky anions.[23]

The MD result gives us insight into the intermolecular interactions of H_2O molecules. We analyzed the environment of H_2O molecules in the 0% and 60% PEG electrolyte to reveal the percentage of water molecules which solvate each electrolyte species: other H_2O molecules (i.e., free water), Fe^{2+}, OTf$^-$, PEG, or some combination (Figure 3e). We find that compared to 0% PEG, the 60% PEG system reduces the prevalence of free water from 59.7% to a mere 8.6%. In the 60% PEG electrolyte, over 70% of H_2O molecules are involved with solvating PEG. These results suggest that PEG indeed disrupts the H_2O hydrogen-bonding network, which agrees with the FT-IR and Raman results. This should increase the O−H bond strength within water molecules and increase the HER overpotential, as supported by the GC measurements. As a result, the electrochemical performance is improved, as discussed previously.

X-ray photoelectron spectroscopy (XPS) was employed to examine possible differences between the Fe anode surfaces after cycling in the 0% PEG and of the 60% PEG systems, respectively. We measured samples of Fe plated onto Cu after 10.5 cycles in Fe||Cu half cells. In both systems, fluorine and sulfur are detected on the Fe anode surface, suggesting some decomposition of the OTf$^-$ anion is occurring which contributes to an interphase on the Fe anode (Supplementary Figure 9). However, no significant differences in elemental ratios between the two systems were observed, suggesting that the chemical makeup of any anode interphase is not a primary contributor to the performance differences observed.

After realizing improved electrochemical performance and suppressed HER, we suspect that 60% PEG may have a significant effect on Fe metal nucleation and growth. To investigate this question, we plated 5 μAh cm^{-2} Fe onto a lacey carbon/Cu TEM grid in 0% and 60% PEG electrolyte. With high resolution transmission electron microscopy (TEM), it is difficult to observe clearly crystalline regions in the control 0%

PEG electrolyte (Figure 4a). When we do locate crystalline regions, they are highly defective and we were unable to assign consistent *d*-spacings (Figure 4b). We also plated a relatively high capacity of 3 mAh cm^{-2} Fe on Cu foil to observe the growth morphology using scanning electron microscopy (SEM). With energy dispersive X-ray spectroscopy (EDS) (Supplementary Figure 10) combined with the evidence of Fe plating from XRD, we find that Fe metal grows with high surface area and sharp surfaces (Figure 4c). It appears that in 0% PEG electrolyte, Fe nucleation and growth is disrupted which leads to defective and random morphology.

In contrast, after plating 5 μAh cm^{-2}, the 60% PEG electrolyte yields well-defined Fe nuclei of about 10 nm in diameter (Figure 4d). We observe a hexagonal atomic arrangement and *d*-spacing of 0.203 nm corresponding to the $1\bar{1}0$ plane down the 111 zone axis of Fe metal (Figure 4e). When imaging a higher plating capacity of 3 mAh cm^{-2} with SEM, we find that, compared to the 0% PEG electrolyte, the 60% PEG electrolyte yields larger Fe crystals with a smoother, more compact Fe morphology (Figure 4f and Supplementary Figure 11). XRD pole figure analysis of Fe plated on Cu (0.2 mA cm^{-2}; 3 mAh Fe cm^{-2}) reveals that the α-Fe (110) planes in both systems grow preferentially from 0° (parallel) to about 45° relative to the Cu substrate (Supplementary Figure 12). Notably, the PEG imparts a more uniform texture compared to the control 0% PEG electrolyte. Overall, Fe nucleation and growth is more crystalline and controlled in 60% PEG electrolyte compared to that in the 0% PEG electrolyte.

The larger Fe particle size plated in the presence of PEG can be understood in part by examining the difference between the nucleation and growth overpotentials. As discussed by Pei et al.,[35] when nucleation overpotential is greater than growth overpotential, instantaneous nucleation occurs followed by particle growth via deposition onto existing nuclei. We observed in the first plating of Fe onto Cu (Figure 2b) that nucleation in 60% PEG occurred at −430 mV vs Fe^{2+}/Fe, after which the overpotential is largely decreasing and lowers to −400 mV by the end of this first plating step. However, a different trend is observed in the 0% PEG case. The overpotential at nucleation appears around −335 mV, and after an initial dip, the overpotential continues to climb past the nucleation overpotential to −348 mV by the end of the first plating. This trend suggests that nucleation in the system without PEG is more progressive, which would lead to more particles of a smaller size. With PEG, nucleation appears to be more instantaneous, which helps explain the fewer but larger particles observed in the 60% PEG electrolyte. In addition, because PEG suppresses HER, Fe nucleation and growth may proceed with less disruption from H_2 bubble formation at the anode/electrolyte interface. This effect can also contribute to the more crystalline nuclei and larger particle sizes observed in the PEG case. The compact, lower surface area morphology is beneficial for higher energy density anodes and means fewer sites for the HER, thus contributing to efficient Fe plating/stripping.

In summary, we apply the molecular crowding strategy to Fe metal anodes and find that adding PEG strengthens intramolecular O−H bonds of water, improves Fe anode efficiency, suppresses HER, and enables more crystalline and compact Fe nucleation and growth. This work demonstrates the effectiveness of crowding agents in the electrolyte for Fe metal anodes operating under a plating/stripping mechanism. Future efforts should focus on fine-tuning the cosolvents for higher ionic conductivity, which should allow for lower overpotentials and better cation mobility. The effect of the electrolyte salt anion on the Fe efficiency and morphology should also be explored. Optimizing the chemistry of these electrolyte components will allow for further improvement of the Fe metal anode performance at a low cost.

■ ASSOCIATED CONTENT

Supporting Information

The Supporting Information is available free of charge at https://pubs.acs.org/doi/10.1021/acsenergylett.4c03268.

> Raman spectrum, viscosity measurement, X-ray diffraction measurements of Fe metal, voltage profiles, MD simulation snapshots and radial distribution functions, XPS of plated Fe, SEM-EDS of plated Fe, XRD pole figure of plated Fe, and experimental details (PDF)

■ AUTHOR INFORMATION

Corresponding Author

Yi Cui − *Department of Materials Science and Engineering and Department of Energy Science and Engineering, Stanford University, Stanford, California 94305, United States; Stanford Institute for Materials and Energy Sciences, SLAC National Accelerator Laboratory, Menlo Park, California 94025, United States;* orcid.org/0000-0002-6103-6352; Email: yicui@stanford.edu

Authors

Louisa C. Greenburg − *Department of Materials Science and Engineering, Stanford University, Stanford, California 94305, United States;* orcid.org/0000-0002-0545-0081

John Holoubek − *Department of Materials Science and Engineering, Stanford University, Stanford, California 94305, United States;* orcid.org/0000-0003-0015-4512

Yi Cui − *Department of Materials Science and Engineering, Stanford University, Stanford, California 94305, United States*

Pu Zhang − *Department of Materials Science and Engineering, Stanford University, Stanford, California 94305, United States*

Huayue Ai − *Department of Chemistry, Stanford University, Stanford, California 94305, United States;* orcid.org/0009-0009-0017-8881

Elizabeth Zhang − *Department of Materials Science and Engineering, Stanford University, Stanford, California 94305, United States*

Chenwei Liu − *Department of Materials Science and Engineering, Stanford University, Stanford, California 94305, United States*

Guangxia Feng − *Department of Materials Science and Engineering, Stanford University, Stanford, California 94305, United States*

Complete contact information is available at: https://pubs.acs.org/10.1021/acsenergylett.4c03268

Author Contributions

Y.C. (corresponding author) supervised the project. Y.C. (corresponding author) and L.C.G. conceived the project. L.C.G. designed and carried out the experiments. J.H. assisted with GC measurement and conducted computational simulations. Y.C. (coauthor) conducted TEM measurement. P.Z. conducted XRD pole figure measurement. H.A. assisted with pouch cell fabrication. E.Z. conducted viscosity measurement. C.L. and G.F. assisted with cell fabrication. All authors discussed the results and commented on the manuscript.

Notes

The authors declare no competing financial interest.

■ ACKNOWLEDGMENTS

This work is supported by the Aqueous Battery Consortium, an energy innovation hub under the US Department of Energy, Office of Basic Energy Sciences, Division of Materials Science and Engineering. The electron microscopy works are supported by the cryo-EM FWP from the US Department of Energy, Office of Basic Energy Sciences, Division of Materials Science and Engineering under contract DE-AC02-76SF00515. Part of this work was performed at the Stanford Nano Shared Facilities (SNSF) RRID:SCR_023230, supported by the National Science Foundation under award ECCS-2026822. L.C.G. acknowledges support from the National Science Foundation Graduate Research Fellowship under Grant 2146755.

■ REFERENCES

(1) Wu, X.; Markir, A.; Xu, Y.; Zhang, C.; Leonard, D. P.; Shin, W.; Ji, X. A Rechargeable Battery with an Iron Metal Anode. *Adv. Funct Materials* **2019**, *29* (20), No. 1900911.

(2) He, Z.; Xiong, F.; Tan, S.; Yao, X.; Zhang, C.; An, Q. Iron Metal Anode for Aqueous Rechargeable Batteries. *Materials Today Advances* **2021**, *11*, No. 100156.

(3) Sandstrom, S. K.; Ji, X. Unlocking the Longevity of the Iron Metal Anode. *ACS Cent. Sci.* **2022**, *8* (6), 686−688.

(4) Yadav, J. K.; Rani, B.; Saini, P.; Dixit, A. A High-Performance and Fast-Charging Rechargeable Iron-Ion Battery Using V $_2$ O $_5$ Porous Microspheres Cathode. *Energy Tech* **2024**, *12*, No. 2401334.

(5) *Iron and Steel Scrap in December 2023*; Mineral Industry Surveys; United States Geological Survey, 2024.

(6) *Zinc in December 2023*; Mineral Industry Surveys; United States Geological Survey, 2024.

(7) Oarga-Mulec, A.; Luin, U.; Valant, M. Back to the Future with Emerging Iron Technologies. *RSC Adv.* **2024**, *14* (29), 20765−20779.

(8) Jiang, J.; Liu, J. *Iron Anode-Based Aqueous Electrochemical Energy Storage Devices: Recent Advances and Future Perspectives* **2022**, *1*, 116.

(9) Sui, Y.; Ji, X. Anticatalytic Strategies to Suppress Water Electrolysis in Aqueous Batteries. *Chem. Rev.* **2021**, *121* (11), 6654−6695.

(10) Inoue, K.; Nakata, T.; Watanabe, T. Surface Morphology and Crystallographic Orientation of Electrodeposited Iron Films. *Mater. Trans.* **2002**, *43* (6), 1318−1324.

(11) Díaz, S. L.; Calderón, J. A.; Barcia, O. E.; Mattos, O. R. Electrodeposition of Iron in Sulphate Solutions. *Electrochim. Acta* **2008**, *53* (25), 7426−7435.

(12) Hawthorne, K. L.; Petek, T. J.; Miller, M. A.; Wainright, J. S.; Savinell, R. F. An Investigation into Factors Affecting the Iron Plating Reaction for an All-Iron Flow Battery. *J. Electrochem. Soc.* **2015**, *162* (1), A108−A113.

(13) Liu, J.; Dong, D.; Caro, A. L.; Andreas, N. S.; Li, Z.; Qin, Y.; Bedrov, D.; Gao, T. Aqueous Electrolytes Reinforced by Mg and Ca Ions for Highly Reversible Fe Metal Batteries. *ACS Central Science* **2022**, *8* (6), 729−740.

(14) Wu, W.; Yang, X.; Wang, K.; Li, C.; Zhang, X.; Shi, H.-Y.; Liu, X.-X.; Sun, X. Regulating the Electro-Deposition Behavior of Fe Metal Anode and the Applications in Rechargeable Aqueous Iron-Iodine Batteries. *Chemical Engineering Journal* **2022**, *432*, No. 134389.

(15) Xie, J.; Liang, Z.; Lu, Y. C. Molecular Crowding Electrolytes for High-Voltage Aqueous Batteries. *Nat. Mater.* **2020**, *19* (9), 1006−1011.

(16) Sun, P.; Ma, L.; Zhou, W.; Qiu, M.; Wang, Z.; Chao, D.; Mai, W. Simultaneous Regulation on Solvation Shell and Electrode Interface for Dendrite-Free Zn Ion Batteries Achieved by a Low-Cost Glucose Additive. *Angew. Chem. Int. Ed* **2021**, *60* (33), 18247−18255.

(17) Hou, Z.; Lu, Z.; Chen, Q.; Zhang, B. Realizing Wide-Temperature Zn Metal Anodes through Concurrent Interface Stability Regulation and Solvation Structure Modulation. *Energy Storage Materials* **2021**, *42*, 517−525.

(18) Cao, Z.; Zhu, X.; Gao, S.; Xu, D.; Wang, Z.; Ye, Z.; Wang, L.; Chen, B.; Li, L.; Ye, M.; Shen, J. Ultrastable Zinc Anode by Simultaneously Manipulating Solvation Sheath and Inducing Oriented Deposition with PEG Stability Promoter. *Small* **2022**, *18* (6), No. 2103345.

(19) Wu, Y.; Zhu, Z.; Shen, D.; Chen, L.; Song, T.; Kang, T.; Tong, Z.; Tang, Y.; Wang, H.; Lee, C. S. Electrolyte Engineering Enables Stable Zn-Ion Deposition for Long-Cycling Life Aqueous Zn-Ion Batteries. *Energy Storage Materials* **2022**, *45*, 1084−1091.

(20) Chen, Y.; Guo, S.; Qin, L.; Wan, Q.; Pan, Y.; Zhou, M.; Long, M.; Fang, G.; Liang, S. Low Current-Density Stable Zinc-Metal Batteries Via Aqueous/Organic Hybrid Electrolyte. *Batteries & Supercaps* **2022**, *5* (5), No. e202200001.

(21) Ciurduc, D. E.; Cruz, C. de la; Patil, N.; Mavrandonakis, A.; Marcilla, R. Molecular Crowding Bi-Salt Electrolyte for Aqueous Zinc Hybrid Batteries. *Energy Storage Materials* **2022**, *53*, 532−543.

(22) Yu, M.; Zhao, S. S.; Xiao, Y.; Zhang, R.; Liu, L.; Chen, S. High-Performance Zinc-Ion Battery Enabled by Tuning the Terminal Group and Chain Length of PEO-Based Oligomers. *Batteries and Supercaps* **2023**, *6* (3), e202200535.

(23) Ciurduc, D. E.; de la Cruz, C.; Patil, N.; Mavrandonakis, A.; Marcilla, R. An Improved PEG-Based Molecular Crowding Electrolyte Using Zn(TFSI)2 vs. Zn(OTf)2 for Aqueous Zn//V2O5 Battery. *Materials Today Energy* **2023**, *36*, 101339.

(24) Li, D.; Cao, L.; Deng, T.; Liu, S.; Wang, C. Design of a Solid Electrolyte Interphase for Aqueous Zn Batteries. *Angew. Chem. Int. Ed* **2021**, *60* (23), 13035−13041.

(25) Rooney, R. T.; Schmitt, K. G.; von Horsten, H. F.; Schmidt, R.; Gewirth, A. A. Raman andQCM Studies of PPG and PEG Adsorption on Cu Electrode Surfaces. *J. Electrochem. Soc.* **2018**, *165* (14), D687−D695.

(26) Liu, Z.; El Abedin, S. Z.; Endres, F. Electrochemical and Spectroscopic Study of Zn(II) Coordination and Zn Electrodeposition in Three Ionic Liquids with the Trifluoromethylsulfonate Anion, Different Imidazolium Ions and Their Mixtures with Water. *Phys. Chem. Chem. Phys.* **2015**, *17* (24), 15945−15952.

(27) Wang, Y.; Wang, Z.; Pang, W. K.; Lie, W.; Yuwono, J. A.; Liang, G.; Liu, S.; Angelo, A. M. D.; Deng, J.; Fan, Y.; Davey, K.; Li, B.; Guo, Z. Solvent Control of Water O−H Bonds for Highly Reversible Zinc Ion Batteries. *Nat. Commun.* **2023**, *14* (1), 2720.

(28) Luo, J.; Xu, L.; Yang, Y.; Huang, S.; Zhou, Y.; Shao, Y.; Wang, T.; Tian, J.; Guo, S.; Zhao, J.; Zhao, X.; Cheng, T.; Shao, Y.; Zhang, J. Stable Zinc Anode Solid Electrolyte Interphase via Inner Helmholtz Plane Engineering. *Nat. Commun.* **2024**, *15* (1), 6471.

(29) Du, H.; Dong, Y.; Li, Q.; Zhao, R.; Qi, X.; Kan, W.; Suo, L.; Qie, L.; Li, J.; Huang, Y. A New Zinc Salt Chemistry for Aqueous Zinc-Metal Batteries. *Adv. Mater.* **2023**, *35* (25), No. 2210055.

(30) Kim, J.-W.; Lee, J.-Y.; Park, S.-M. Effects of Organic Additives on Zinc Electrodeposition at Iron Electrodes Studied by EQCM and in Situ STM. *Langmuir* **2004**, *20* (2), 459−466.

(31) Qian, J.; Henderson, W. A.; Xu, W.; Bhattacharya, P.; Engelhard, M.; Borodin, O.; Zhang, J.-G. High Rate and Stable Cycling of Lithium Metal Anode. *Nat. Commun.* **2015**, *6* (1), 6362.

(32) Yu, Z.; Wang, H.; Kong, X.; Huang, W.; Tsao, Y.; Mackanic, D. G.; Wang, K.; Wang, X.; Huang, W.; Choudhury, S.; Zheng, Y.; Amanchukwu, C. V.; Hung, S. T.; Ma, Y.; Lomeli, E. G.; Qin, J.; Cui, Y.; Bao, Z. Molecular Design for Electrolyte Solvents Enabling Energy-Dense and Long-Cycling Lithium Metal Batteries. *Nat. Energy* **2020**, *5* (7), 526−533.

(33) Yu, Z.; Rudnicki, P. E.; Zhang, Z.; Huang, Z.; Celik, H.; Oyakhire, S. T.; Chen, Y.; Kong, X.; Kim, S. C.; Xiao, X.; Wang, H.; Zheng, Y.; Kamat, G. A.; Kim, M. S.; Bent, S. F.; Qin, J.; Cui, Y.; Bao, Z. Rational Solvent Molecule Tuning for High-Performance Lithium Metal Battery Electrolytes. *Nat. Energy* **2022**, *7* (1), 94−106.

(34) Oyakhire, S. T.; Liao, S.-L.; Shuchi, S. B.; Kim, M. S.; Kim, S. C.; Yu, Z.; Vilá, R. A.; Rudnicki, P. E.; Cui, Y.; Bent, S. F. Proximity Matters: Interfacial Solvation Dictates Solid Electrolyte Interphase Composition. *Nano Lett.* **2023**, *23* (16), 7524−7531.

(35) Pei, A.; Zheng, G.; Shi, F.; Li, Y.; Cui, Y. Nanoscale Nucleation and Growth of Electrodeposited Lithium Metal. *Nano Lett.* **2017**, *17* (2), 1132−1139.